

# An Electrochemical Microbubble-Based MEMS Pressure Sensor

Lawrence Yu, Christian A. Gutierrez, and Ellis Meng, *Senior Member, IEEE*

**Abstract**—A novel pressure transducer concept is introduced in which external pressure variations induce changes in the volume of a trapped microbubble ( $\mu\text{B}$ ) in an electrolyte solution. These volumetric changes are monitored by electrochemical impedance-based measurements and may be used for pressure tracking applications. Microbubbles are nucleated on-demand by electrolysis within a confinement chamber with high precision (measured size RSD  $\sim 1\%$ ). This pressure transducer concept was developed specifically for operation in liquid environments and features biocompatible construction, small footprint ( $<0.1 \text{ mm}^2$ ), and low power consumption ( $<1 \text{ nW}$ ). This combination of features is ideal for *in vivo* pressure monitoring applications. [2015-0203]

**Index Terms**—Pressure measurement, electrochemical device, impedance-based sensing, Parylene C, electrochemical-microelectromechanical systems (EC-MEMS).

## I. INTRODUCTION

CHRONICALLY implantable transducers enable around the clock monitoring of localized *in vivo* pressures [2]–[4], a useful indicator of patient health or disease progression. One region where hydrostatic pressure is highly regulated is within the skull [5], [6]. For those with hydrocephalus, this ability to regulate intracranial pressure (ICP) is impaired and potentially life threatening [8]. Treatment involves the implantation of a catheter to shunt the excess cerebrospinal fluid (CSF) into another region of the body where it can be safely processed [10], but failures occur at a high rate [11], [12] and there is currently no way to reliably and accurately monitor shunt status noninvasively. Current clinical practice to interrogate ICP involves lumbar infusion and tapping into the shunt reservoir, which is accurate but invasive [13]–[15]. Meanwhile, noninvasive imaging techniques (ultrasound, MRI) do not provide the accuracy necessary for clinical use [16]–[19]. Sensors can

Manuscript received July 17, 2015; revised October 1, 2015; accepted November 4, 2015. Date of publication November 22, 2015; date of current version February 1, 2016. This work was supported by the National Science Foundation through the Division of Electrical, Communications, and Cyber Systems under Grant ECCS-1231994. Subject Editor D. Devoe.

L. Yu is with the Biomedical Engineering Department, University of Southern California, Los Angeles, CA 90089 USA (e-mail: lawrence.yu@usc.edu).

C. A. Gutierrez was with the University of Southern California, Los Angeles, CA 90089 USA. He is now with Google Inc., Mountain View, CA 94035 USA (e-mail: chris.a.gutierrez@gmail.com).

E. Meng is with the Biomedical Engineering and Electrical Engineering Department, University of Southern California, Los Angeles, CA 90089 USA (e-mail: ellis.meng@usc.edu).

Color versions of one or more of the figures in this paper are available online at <http://ieeexplore.ieee.org>.

Digital Object Identifier 10.1109/JMEMS.2015.2499167

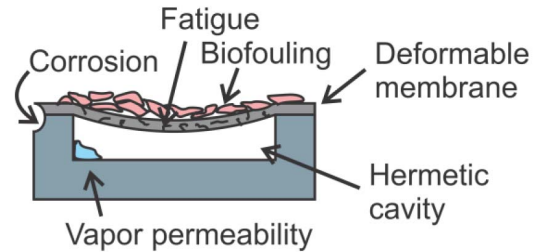


Fig. 1. Cartoon of commonly utilized deflecting diaphragm based transduction mechanism and several possible failure modes.

be implanted during the shunting surgery and provide the promise of accurate, noninvasive monitoring through telemetry. These microfabricated sensors typically comprise an air cavity sealed with a thin, flexible membrane that deflects upon application of external pressure [20]. Examples of this transduction principle were implemented in early MEMS (microelectromechanical systems) sensors [21] and can be found today in a FDA approved implanted pressure transducer (CardioMEMS, St. Jude Medical, MN, USA). Despite advances in sensor development, the inhospitable *in vivo* environment remains a formidable challenge, where the corrosive aqueous environment and foreign body response [22] can cause eventual degradation of hermetic packaging or obscure transducing elements and induce sensor drift (Figure 1).

To address these issues, alternative approaches have been investigated involving the use of trapped gases in liquid for pressure sensing. Instead of measuring membrane deflection, the geometry of the liquid-gas boundary is observed as it changes with pressure [23]–[26]. This sensing principle harnesses the liquid environment, does not require hermetic packaging, and is immune to biofouling. This work utilizes precisely generated single microbubbles that are localized within a microfabricated confinement structure to track pressure by measuring their pressure-responsive size changes using electrochemical impedance. The exclusive use of polymer materials has the additional benefits of reduced complexity, mechanical flexibility, and streamlined integration for other medical applications.

## II. DESIGN

The microbubble pressure transducer ( $\mu\text{BPT}$ ) utilizes a pair of platinum electrodes embedded within a Parylene C microstructure to first electrolytically generate a microbubble and then subsequently measure its size and dissolution rate through the use of electrochemical impedance

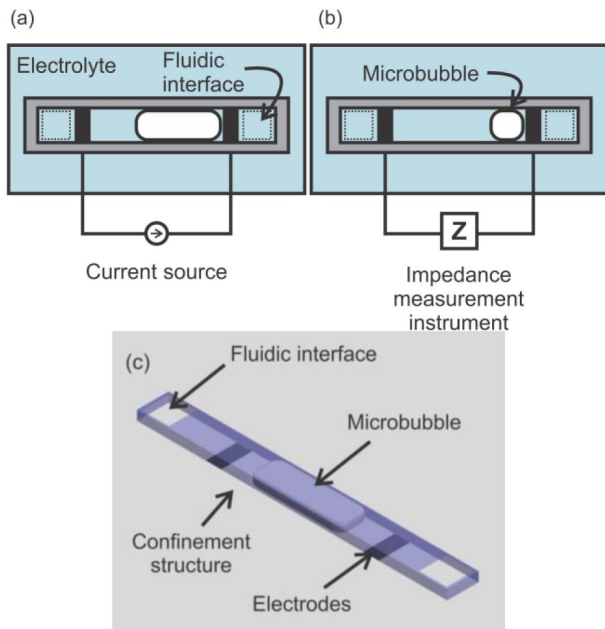


Fig. 2. Cartoon of device operation, illustrating top down view of Parylene microstructure filled in electrolyte. (a) Nucleation of microbubble via electrolysis. (b) Impedance measurement of microbubble during dissolution. (c) 3D rendering of  $\mu$ BPT, illustrating confinement of microbubble.

measurement (Figure 2). Parylene (USP class VI polymer and inert) and platinum construction is highly biocompatible [22], serves as an excellent electrical insulator, and possesses great mechanical strength [27], [28].

Bubble nucleation is commonly implemented through a phase change with a heating element (boiling) [29] or through a Faradaic charge transfer reaction (electrolysis) [30]. Considering restrictions on power and local heat generation for biological implants, electrolysis was selected for this application. Detection of microbubble size has been implemented through a variety of methods (i.e. ultrasonic, optical); the electrochemical impedance sensing modality was selected because it can be performed using the same electrode pair that generates the microbubble.

Microbubbles in contact with a hydrophobic surface (such as that of Parylene C) are in an energetically favorable state and resist detachment [31]. Device orientation becomes an important consideration if buoyancy forces acting upon microbubbles are sufficiently large to carry them away from sensing electrodes. Postural changes occur frequently and have a noted effect on ICP, so sensor orientation dependence must be minimized. A chamber is also necessary to create a localized environment for the saturation of electrolytically generated gas. The ability to isolate and control the conditions in this environment allows for consistent electrochemical measurements. Thus, a confinement chamber was designed to localize microbubbles while maintaining an open connection to the surrounding liquid environment.

Despite the widespread use of electrochemical detection techniques in biological analysis systems, examples of electrochemical (EC) based sensing technologies used for measurement of physical quantities such as force and pressure has been limited. The potential of impedance based

transduction of pressure using a fluid filled sensor was first described by Ateya *et al.* through the use of bubbles formed in silicon microchannels encapsulated in polydimethylsiloxane (PDMS) [32]. However, the device was confined to a rigid substrate with bulky fluidic interconnects and not suitable for *in vivo* implantation. The open-sensor design and all Parylene construction of this approach simplifies implementation and obviates requirements of hermeticity. To our knowledge, this approach is the first application of such a sensing modality to microfabricated polymer-based transducers.

The performance metrics of existing *in vivo* pressure transducer technologies can be used to guide sensor design. Physiologically relevant pressures in hydrocephalus patients falls between 6.6 to 13.3 kPa (commonly reported units:  $-50$  to  $100$  mmHg) and are taken as a gauge measurement with respect to atmospheric pressure with a supine patient. The neuroanatomy of the central nervous system (brain and spine) is bathed in CSF, an incompressible liquid. The addition of a microbubble (10 orders of magnitude smaller in volume compared to cranial compartment) can be used to intermittently track the pressure within the cranial compartment.

### III. THEORETICAL CONSIDERATIONS

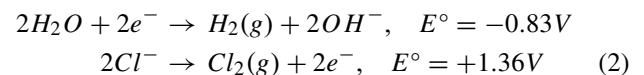
#### A. Electrolytic Microbubble Nucleation

Faraday's laws of electrolysis described the relationship between the mass of a substance altered at an electrode during electrolysis and the quantity of electricity delivered to the electrode. With the application of a constant current for electrolysis, the relationship can be described as [33]:

$$n = \frac{It_e}{Fz} \quad (1)$$

where  $n$  represents the amount of substance altered (in moles),  $I$  is the magnitude of the applied current,  $t_e$  is the duration of the current application,  $F$  is the Faraday constant, and  $z$  the valence number of the substance.

The liquid medium contained in the confinement structure must be an electrolyte in order to transduce pressure as a function of the size of the bubble which affects the volumetric conduction path. Common examples found *in vivo* are CSF, blood, and tears. Within phosphate buffered saline (PBS), a commonly used electrolyte to mimic the conditions found *in vivo*, the predominant electrolysis reactions are as follows [34]:



Bubble nucleation results in ion concentration and pH gradients; typical electrolysis events generate subnanomolar ( $\sim 10^{-11}$ ) concentration gradients that can be readily neutralized by buffering.

#### B. Microbubble Dynamics

The fluid dynamics of a spherical bubble suspended in an infinitely large body of liquid are described by the Rayleigh-Plesset equation [24]:

$$r\ddot{r} + \frac{3}{2}\dot{r}^2 = \frac{1}{\rho_d} \left( p_g - p_\infty - \frac{2\sigma}{r} - \frac{4\mu}{r}\dot{r} \right) \quad (3)$$

where  $r$  represents the bubble radius as a function of time (dots denote time derivatives);  $p_g$  and  $p_\infty$  are the pressure of the gas within the bubble boundary and the external pressure taken at a distance infinitely far away from the bubble, respectively;  $\sigma$  denotes surface tension;  $\mu$  represents fluid viscosity; and  $\rho_d$  is fluid density. For pressure oscillation frequencies significantly lower than the bubble resonant frequency, the pressure-radius relationship can be described as [24], [35]:

$$p_\infty = p_i \left( \frac{r_0}{r} \right)^b - \frac{2\sigma}{r} \quad (4)$$

With the polytropic exponent  $b \approx 1$ , the equation resembles the Young-Laplace equation and describes the balance of forces at the gas-liquid interface due to surface tension and external pressure. For CSF, the surface tension is relatively constant and homogeneous, and thus the bubble size can be directly correlated to the external pressure. During dissolution, hydrostatic pressure exerts forces normal to the liquid-gas boundary, where the geometry is dictated by the shape of the microbubble confinement chamber. Within the confines of a hydrophobic Parylene [22] microstructure, the gas exhibits nonlinear dissolution characteristics due to effects of the surface chemistry on surface tension [36].

At larger time scales, the gas within the bubble will dissolve into the surrounding under-saturated liquid, as governed by Henry's law:

$$c_\infty = ap_g \quad (5)$$

where  $c_\infty$  is the concentration of the dissolved gas in the bulk liquid,  $a$  is a temperature dependent constant (also known as Henry's law constant) characteristic of the particular gas-liquid combination, and  $p_g$  is the partial pressure of the gas acting on the liquid surface (i.e. the gas within the bubble). For a fixed external pressure (e.g. the regulated ICP of a normal patient), the gas concentration  $c$  must satisfy (5) for the gas within the bubble to remain in equilibrium with the surrounding liquid, else the bubble will grow or shrink in size. The effects of gas dissolution on bubble size was described by Epstein and Plesset [37]:

$$\frac{dr}{dt} = \frac{k(c_s - c_\infty)}{\rho_\infty + 2\tau/3r} \left( \frac{1}{r} + \frac{1}{(\pi kt)^{1/2}} \right) \quad (6)$$

where  $k$  is the diffusion coefficient (see TABLE 1 for examples) of the specific gas-liquid combination,  $c_s$  is the saturation concentration of gas in the liquid at the bubble surface,  $\rho_\infty$  is the density of the gas within the bubble, and  $\tau$  is the modified surface tension. The primary product in the electrolysis of PBS as described in (2) is  $H_2$ , thus we expect the diffusion coefficient to be near that of the  $H_2$ - $H_2O$  combination (TABLE 1). This diffusion process is limited by mass transfer and is relatively slow; the typical dissolution rate of bubbles with radius  $100 \mu\text{m}$  are estimated to be on the order of  $\sim 0.1 \mu\text{m/s}$ .

### C. Electrochemical Sensing

The electrochemical impedance of an electrolyte as measured by immersed microelectrodes can be represented by the well-known Randles circuit model (Figure 3) [38].

TABLE I  
DIFFUSION COEFFICIENTS OF GAS-LIQUID COMBINATIONS

Solute-solvent combination	Diffusion coefficient at 25°C (cm <sup>2</sup> /s)
H <sub>2</sub> -H <sub>2</sub> O	4.50 × 10 <sup>-5</sup> [1]
O <sub>2</sub> -H <sub>2</sub> O	2.10 × 10 <sup>-5</sup> [1]
Air-NaCl (aq.)	2.5 × 10 <sup>-5</sup> [7]
Cl <sub>2</sub> -H <sub>2</sub> O	1.38 × 10 <sup>-5</sup> [9]

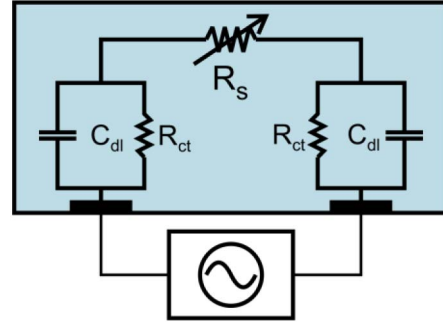


Fig. 3. Simplified Randles circuit model of electrodes in electrolyte.

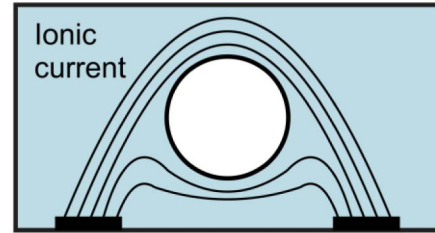


Fig. 4. Electrochemical measurement of bubble size in electrolyte.

Impedance is measured using an alternating current signal at sufficiently high frequencies such that the solution resistance dominates the impedance response. The complex impedance is reduced to its real component and can be represented using the DC model, where resistance is inversely proportional to the cross-sectional area between electrodes, as described by the following:

$$|Z|_{f \geq 10kHz} \approx R_s = \frac{\rho_e l}{S_{Tot}} \quad (7)$$

where  $Z$  is the complex impedance measured by the electrodes,  $R_s$  is the solution resistance,  $\rho_e$  is the resistivity of the electrolyte,  $l$  the distance between electrodes, and  $S_{Tot}$  the effective cross sectional area of the ionic conduction path. A suspended microbubble behaves as a nonconductive void within the conductive electrolyte (Figure 4), altering the cross-sectional area and thus the overall solution resistance. This phenomenon enables the transduction and measurement of hydrostatic pressure acting upon microbubble size. The sensitivity of the device is dependent on electrode arrangement, sensor dimensions, and the volume of electrolyte subject to ionic current flow.

The geometry of the gas-liquid interface and ionic conduction path is largely dictated by the microbubble confinement structure. Rectangular and cylindrical confinement

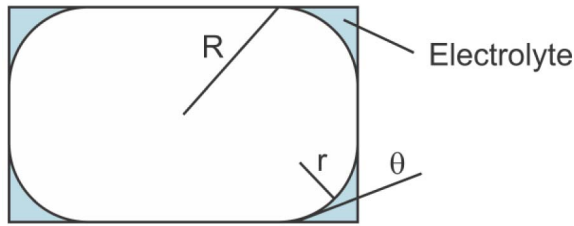


Fig. 5. Cross section of bubble in rectangular fluid channel.

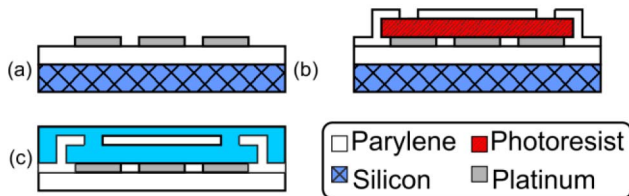


Fig. 6. Cartoon of simplified fabrication process; steps depict cross section view. (a) Deposition of Parylene and Pt lift-off. (b) Patterning of sacrificial photoresist, deposition of Parylene, and fluidic interface port etch. (c) Release device from silicon substrate and soak in electrolyte to fill confinement structure.

chambers were fabricated and evaluated [39]. The geometry of a microbubble confined within a cylindrical chamber is radially symmetric and allows for orientation independent operation. When a microbubble is trapped within a chamber with rectangular cross section, the gas tends to fill the middle of the cross sectional area and leave pockets of liquid at the corners (Figure 5). The cross section profile does not change significantly as the bubble changes in size, while the length of the conduction path changes. As described by Ateya *et al.* [32], the area of this cross section is described as follows:

$$S_{Tot} = 4A \frac{r^2}{R^2} \left[ \frac{\cos \theta}{\sin \pi/4} \cos(\pi/4 + \theta) - (\pi/4 - \theta) \right] \quad (8)$$

where  $A$  is the total cross sectional area of the channel,  $R$  is the inscribed inner radius of the channel,  $r$  the radius of curvature of the corner meniscus, and  $\theta$  the contact angle of the microbubble with the chamber wall. This type of ionic conduction path improves sensitivity by leveraging large changes in impedance observed in the submicrometer sized liquid capillaries found at the corners.

#### IV. FABRICATION

The device was fabricated using surface micromachining techniques on a polymer substrate with thin film electrodes, a process based on previously reported techniques (Figure 6) [40]. The entire fabrication process was performed at relatively low temperatures ( $<90^\circ\text{C}$ ) to prevent thermal degradation of Parylene.

A layer of Parylene ( $12 \mu\text{m}$ , Specialty Coating Systems, Indianapolis, IN) was deposited onto a silicon wafer, which serves as a temporary support substrate. Platinum was deposited ( $2000 \text{ \AA}$  thick) via an electron beam evaporator and features were defined using a lift-off process to form electrodes and traces. An additional  $12 \mu\text{m}$  of Parylene was deposited to serve as an insulation layer. To expose the electrode active areas, the insulation area was removed by the

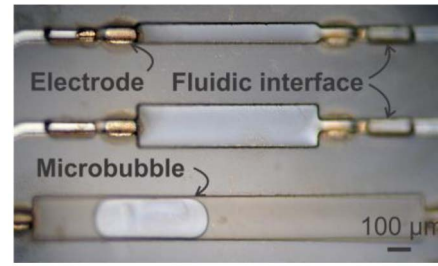


Fig. 7. Micrograph of fabricated devices, with various microchannel confinement structures to enable testing of various electrolyte parameters.

use of switched-chemistry deep reactive ion etching (DRIE) in oxygen plasma [41] with a dual layer photoresist mask ( $15 \mu\text{m}$ , AZ4620; AZ Electronic Materials, Branchburg, NJ). Next, photoresist was patterned ( $10 \mu\text{m}$ , AZ4620) to serve as a sacrificial mold for the microbubble confinement structure. A final  $4 \mu\text{m}$  thick layer of Parylene was deposited to enclose the sacrificial photoresist structure, and access ports were patterned and opened with oxygen plasma reactive ion etching (RIE). Another switched-chemistry DRIE process was performed to etch down to the underlying silicon wafer, forming the die outlines for device release. The remainder of the etch mask and sacrificial structure PR were stripped by soaking the wafer in an acetone bath. By submerging the wafer in water, free film devices were released and separated from the underlying silicon substrate (Figure 7). It is worthy to note that the confinement structures did not experience stiction upon drying.

A robust, epoxyless, reversible electrical connection scheme was established [42], minimizing handling of the thin Parylene devices. A hinge-based zero insertion force (ZIF) connector for flat flexible ribbon cables was utilized (Hirose Electric Co., Simi Valley, CA), enabling a secure connection to be established with the exposed contact pads (8 or 12 channel with  $0.5 \text{ mm}$  pitch). Because the connector mandates a cable thickness of  $300 \mu\text{m}$ , the free film Parylene devices were affixed to a  $0.01 \text{ inch}$  ( $\sim 250 \mu\text{m}$ ) thick polyetheretherketone (PEEK) sheet with a cyanoacrylate based adhesive (All Purpose Crazy Glue, Westerville, OH) and cut down to fit into the connector. The ZIF connector was directly soldered onto a commercially available polymer flexible cable (Molex Inc., Lisle, IL). The use of this thicker, more robust polymer cable results in a secure, repeatable connection to a measurement printed circuit board (PCB) via another ZIF connector.

#### V. EXPERIMENTAL METHODS

Multiplexing circuitry (Analog Devices ADG1206; Norwood, MA) was utilized to control device connections to instrumentation and facilitate usage of multiple devices on the same die. Because current injection during electrolysis disrupts impedance measurement, device connections were time division multiplexed between the current source (Keithley Model 2400 Sourcemeter; Keithley Instruments Inc., Cleveland, OH) and LCR meter (Keysight E4980A, Keysight [formerly Agilent] Technologies, Santa Rosa, CA).

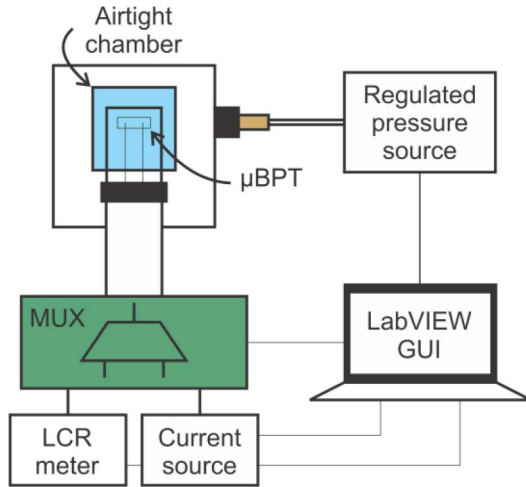


Fig. 8. Schematic overview of test setup, illustrating electrical and fluidic connections.

An acrylic jig with an airtight chamber and fluidic connections was custom fabricated for benchtop characterization of the sensors. Once the devices were mounted, the chamber was purged of air and filled with an electrolyte (e.g.  $1\times$  PBS, artificial cerebrospinal fluid). The jig was connected to a custom built, regulated (ControlAir T900X; ControlAir Inc., Amherst, NH) nitrogen pressure source using PEEK tubing (1/16 in. O.D., 0.055 in. I.D.) prefilled with electrolyte. A commercially available sensor (Omega PX480A) was placed in line to measure the applied pressure during testing.

Multiplexing, pressure regulation, and data acquisition were computer controlled through a LabVIEW based graphical user interface (Figure 8). The devices were placed under a stereomicroscope to provide visual confirmation of device wetting and microbubble generation during benchtop testing. Operation of the sensor can be isolated into separate aspects (electrochemical impedance measurement and electrolytic bubble generation), and each was characterized individually. Afterwards, mechanical response to pressure was evaluated.

## VI. RESULTS

### A. Electrochemical Impedance Measurement

Electrochemical impedance spectroscopy (EIS, 20 Hz–1 MHz) was used to verify and assess electrode surface properties in Fig. 9. Measurement was conducted between adjacent electrodes with a Gamry Reference 600 potentiostat (Gamry Instruments, Warminster, PA). The optimal frequency of measurement ( $f_{\text{measurement}}$ ) where the complex impedance response is dominated by solution resistance, was found to be where the phase response was nearest  $0^\circ$ , corresponding to an excitation frequency of 10 kHz for  $1\times$  PBS (phosphate buffered saline). For this electrochemical impedance measurement, power draw was  $\sim 1$  nW ( $\sim 1$  nA, 1 V<sub>p-p</sub>). Electrochemical impedance measurements are sensitive to parameters such as temperature and concentration of ionic species in the solution. However, both are relatively constant within the cerebrospinal fluid [43], [44].

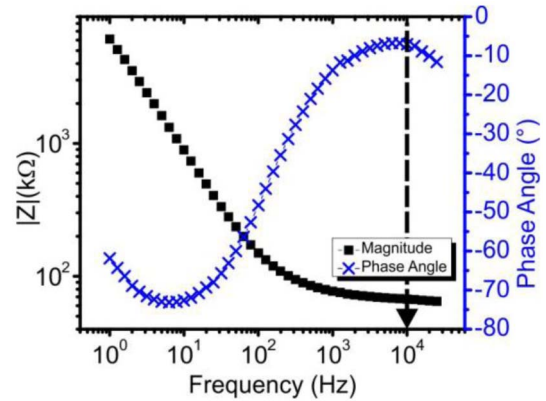


Fig. 9. Electrochemical impedance spectroscopy of sensor response. Arrow indicates measurement frequency, where system is most resistive (minimum phase).

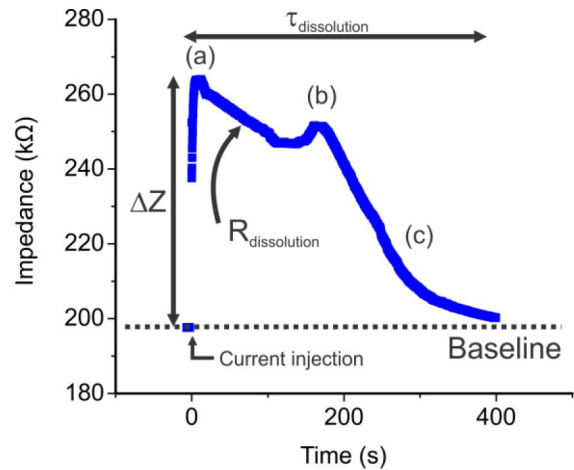


Fig. 10. Representative measurement of electrolytically generated microbubble, with indicators for parameters of interest. (a) Impedance of microbubble immediately following electrolysis. (b) Bubble begins detachment from microchannel. (c) Bubble shrinks rapidly in presence of platinum electrode. Points (a), (b), and (c) correspond to the micrographs in Figure 2.

### B. Electrolytic Bubble Generation

Microbubbles were electrolytically generated by applying direct current pulses ( $1\text{--}5\ \mu\text{A}$  for  $2\text{--}5$  seconds). Impedance monitoring during  $\mu\text{B}$  nucleation enabled precise control of bubble formation [45] and was used to determine the overall charge injection during electrolysis. Optical microscopy was also used to confirm nucleation and containment of the bubble within the microchannel (Figure 11). Electrolysis current was maintained under  $10\ \mu\text{A}$  to avoid delamination of the metal-Parylene interface and for longevity of device [46]. Observed power draw was  $<60\ \mu\text{W}$  for electrolytic bubble generation. Following application of current, electrochemical impedance measurement was used to verify and quantify the growth of the microbubble.

Electrochemical impedance was recorded prior to ( $\sim 10$  s) and following electrolysis (Figure 10). The recorded impedance prior to nucleation served as a baseline. Immediately following electrolysis, the sharp increase in impedance observed is the result of the nonconductive gas displacing the electrolyte solution. The gases within the microbubble

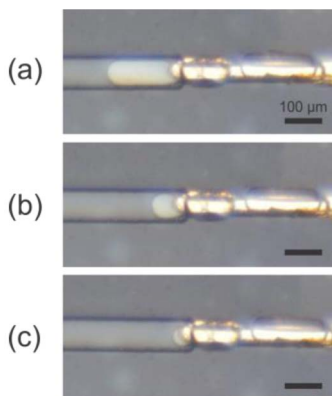


Fig. 11. Micrograph of microbubble dissolution within microchannel. (a) Microbubble immediately following nucleation. (b) Liquid-gas boundary adheres to sidewall of microchannel. (c) Following detachment, microbubble volume diminishes quickly.

gradually diffuse back into solution, thus lowering the measured impedance until its return to baseline. Data was acquired at 5 Hz and was terminated once impedance returned to within 1% of the initial baseline impedance value. Several features of interest (as graphically depicted in Figure 10) were extracted from the temporal impedance response using a MATLAB script. Baseline was defined as the average impedance prior to current injection [ $\Omega$ ],  $\Delta Z$  is the initial impedance response referenced to baseline [ $\Omega$ ],  $R_{\text{dissolution}}$  was defined as the slope within between the (a) and (b) regions in the impedance response as depicted in Figure 10. The dissolution time  $\tau_{\text{dissolution}}$  was defined as the time elapsed from the current injection to the point when the impedance returns to 5% of  $\Delta Z$ .

The presence of local maxima (e.g. around 200 s in Figure 10) can be explained by interactions of the bubble with the Parylene surface. During dissolution, the liquid-air interface adheres and appears to “stick” to the side-walls of the confinement chamber due to interactions with the surface, leading to increased measured electrochemical impedance [32]. The impedance decreases more rapidly once the microbubble detaches from the channel sidewall (Figure 11b). Several different channel geometries were tested, each of which featured characteristic local minima and maxima in the impedance response due to the differences in channel width which impacts microbubble shape. Dissolution was defined in the region where the microbubble was in contact with the channel sidewalls, the configuration in which the impedance measurement is most sensitive.

### C. Priming of Electrochemical Environment

To maintain consistency between bubble nucleation events, the local electrolyte environment was saturated with dissolved gas by repeatedly injecting current to induce electrolysis. Current injections were performed (Figure 12) and the impedance measurements were taken until  $\tau_{\text{dissolution}}$  was consistent to within 10% (Figure 13). This priming process lasted approximately 50 minutes and only needs to be performed once. The  $\Delta Z$  and  $\tau_{\text{dissolution}}$  (as illustrated by Figure 10) from a primed environment impedance response curve

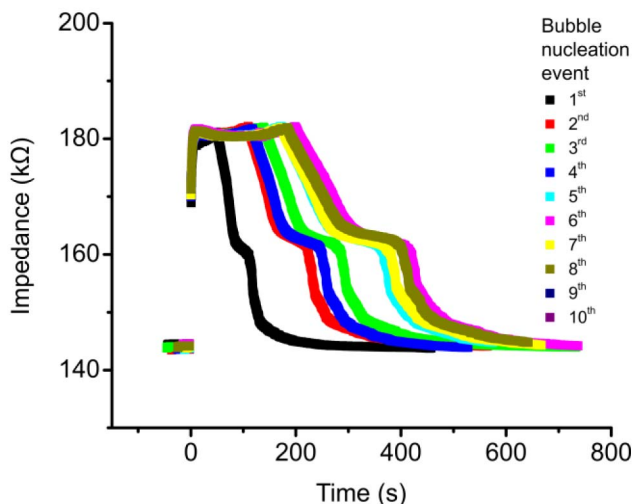


Fig. 12. Successive nucleation events and tracking of microbubble dissolution to establish gas saturation state.

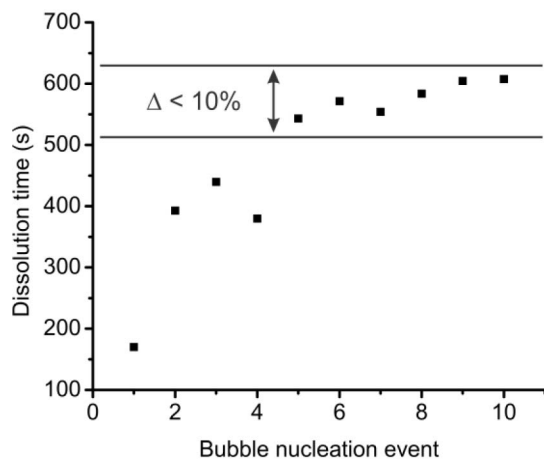


Fig. 13. Tracking stabilization and dissolution time with successive bubble nucleation events.

(i.e. the 5th to 10th current injections in Figure 12) were then analyzed for pressure transduction. Notably, the size of the nucleated bubble remained consistent ( $\sim 1\%$  RSD) while attempting to saturate the local dissolved gas environment, as seen in the low variance of  $\Delta Z$  (mean = 37.9 k $\Omega$ , standard deviation 574.6  $\Omega$ ,  $n = 10$ ).

Note that depressurization of the local environment is another commonly used method to saturate the liquid electrolyte, as utilized by previous studies [47], [48]. However, this method is incompatible with the eventual *in vivo* application and thus was not used for device characterization.

### D. Pressure Transduction

For a given constant pressure environment and set electrolysis parameters, impedance tracking of microbubble size during dissolution was performed (Figure 14). The  $\Delta Z$  metric was observed to have an inversely proportional relationship ( $\Delta Z = 60496 + (1.234E6/(\text{pressure (mmHg)} + 148.85))$ ,  $R^2 = 0.999$ ) to a randomly applied pressure (Figure 15), suggesting that the impedance measurement is a direct measurement of the bubble volume relationship as described by the Young-Laplace

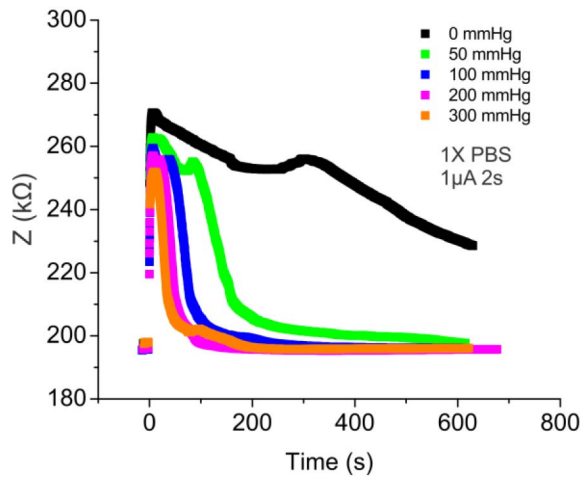


Fig. 14. Measurement of electrolytically generated microbubble and dissolution at various pressures.

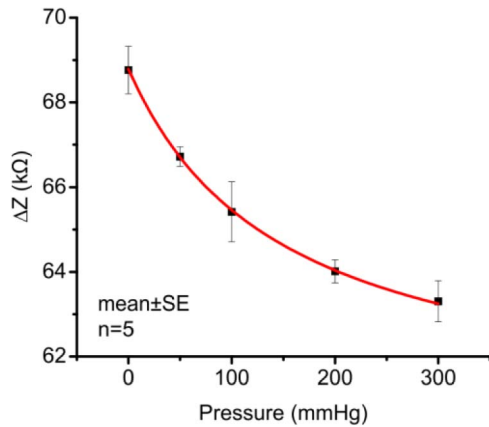


Fig. 15. Initial impedance response  $\Delta Z$ , a direct correlation of microbubble size, in relation to pressure.

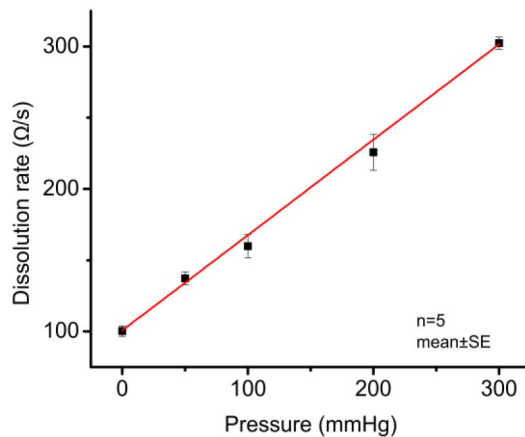


Fig. 16. Dissolution rate in relation to hydrostatic pressure.

equation (4) and Boyle's law. The possibility of absolute pressure monitoring is promising with further calibration of saturation conditions.

Dissolution rate was also shown to have a correlation with pressure (Figure 16). The observed relation was approximately

linear (dissolution rate =  $100.70 + 0.669 \times \text{pressure (mmHg)}$ ,  $R^2 = 0.998$ ), as confirmed by Henry's law (5) and the Epstein-Plesset (6) equations. Provided that the electrochemical measurement is properly primed, this metric provides a method to check the  $\Delta Z$  measurement on the same nucleated microbubble. Using this metric for pressure transduction, the estimated resolution is approximately  $\pm 20$  mmHg.

The range of this sensing modality is dependent on a number of factors and is currently still under investigation. As mentioned in the theoretical considerations section, the amount of injected charge and the dimensions of the confinement chamber directly influence the volume and length of microbubbles. Preliminary pressure measurements at a physiologically relevant range (0-20 mmHg) were achieved by utilizing smaller microbubbles and smaller confinement structures.

## VII. CONCLUSION

Successful development of a unique sensing mechanism for hydrostatic pressure measurement utilizing impedance based measurements of electrolytically generated microbubbles has been demonstrated. Electrochemical impedance measurements within Parylene-based microfluidic structures were possible and demonstrate the feasibility of intracranial pressure measurement. Combined with the exceptional biocompatibility characteristics of the open-to-liquid packaging, this robust sensing mechanism can be used reliably for chronic measurements. Implementation within a completely flexible Parylene substrate has the potential to address the unmet need for reliable, chronic transducers for the monitoring of hydrocephalus treatment. Further calibration of electrolyte saturation characteristics enables usage in a multitude of wet sensing applications.

## ACKNOWLEDGMENT

The authors would like to thank Mr. Jeff Nishida, Mr. Aduragbemi Jibodu, and the members of the USC Biomedical Microsystems Laboratory for their assistance.

## REFERENCES

- [1] E. L. Cussler, *Diffusion: Mass Transfer in Fluid Systems*. Cambridge, U.K.: Cambridge Univ. Press, 2009.
- [2] J. Eom, J. Lee, H. Lee, and B. Choi, "Energy harvesting for bladder pressure sensor using parametric amplification phenomenon of PVDF bimorph cantilever," in *Proc. 6th Biomed. Eng. Int. Conf. (BMEiCON)*, Oct. 2013, pp. 1–3.
- [3] P.-J. Chen, D. C. Rodger, S. Saati, M. S. Humayun, and Y.-C. Tai, "Microfabricated implantable parylene-based wireless passive intraocular pressure sensors," *J. Microelectromech. Syst.*, vol. 17, no. 6, pp. 1342–1351, Dec. 2008.
- [4] M. N. Gulari, M. Ghannad-Rezaie, P. Novelli, N. Chronis, and T. C. Marentis, "An X-ray detectable pressure microsensor for monitoring coronary in-stent restenosis," in *Proc. 27th Int. Conf. MEMS*, San Francisco, CA, USA, Jan. 2014, pp. 893–896.
- [5] P. H. Raboel, J. Bartek, Jr., M. Andresen, B. M. Bellander, and B. Romner, "Intracranial pressure monitoring: Invasive versus non-invasive methods—A review," *Critical Care Res. Pract.*, vol. 2012, Mar. 2012, Art. ID 950393.
- [6] B. Romner and P.-O. Grände, "Traumatic brain injury: Intracranial pressure monitoring in traumatic brain injury," *Nature Rev. Neurol.*, vol. 9, pp. 185–186, Mar. 2013.

- [7] G. Houghton, P. D. Ritchie, and J. A. Thomson, "The rate of solution of small stationary bubbles and the diffusion coefficients of gases in liquids," *Chem. Eng. Sci.*, vol. 17, no. 4, pp. 221–227, 1962.
- [8] N. Arriada and J. Sotelo, "Review: Treatment of hydrocephalus in adults," *Surgical Neurol.*, vol. 58, no. 6, pp. 377–384, 2002.
- [9] A. Tang and O. C. Sandall, "Diffusion coefficient of chlorine in water at 25–60 °C," *J. Chem. Eng. Data*, vol. 30, no. 2, pp. 189–191, 1985.
- [10] A. Aschoff, P. Kremer, B. Hashemi, and S. Kunze, "The scientific history of hydrocephalus and its treatment," *Neurosurgical Rev.*, vol. 22, nos. 2–3, pp. 67–93, 1999.
- [11] J. Kestle *et al.*, "Long-term follow-up data from the shunt design trial," *Pediatric Neurosurgery*, vol. 33, no. 5, pp. 230–236, 2000.
- [12] J. M. Drake *et al.*, "Randomized trial of cerebrospinal fluid shunt valve design in pediatric hydrocephalus," *Neurosurgery*, vol. 43, no. 2, pp. 294–303, 1998.
- [13] J. Zhong, M. Dujovny, H. K. Park, E. Perez, A. R. Perlin, and F. G. Diaz, "Advances in ICP monitoring techniques," *Neurological Res.*, vol. 25, no. 4, pp. 339–350, 2003.
- [14] B. Kahlon, G. Sundbärg, and S. Rehncrona, "Comparison between the lumbar infusion and CSF tap tests to predict outcome after shunt surgery in suspected normal pressure hydrocephalus," *J. Neurol., Neurosurgery Psychiatry*, vol. 73, no. 6, pp. 721–726, 2002.
- [15] J. Woodford, R. L. Saunders, and E. Sachs, Jr., "Shunt system patency testing by lumbar infusion," *J. Neurosurgery*, vol. 45, no. 1, pp. 60–65, 1976.
- [16] Q. Shen, J. Stuart, B. Venkatesh, J. Wallace, and J. Lipman, "Inter observer variability of the transcranial Doppler ultrasound technique: Impact of lack of practice on the accuracy of measurement," *J. Clin. Monitor. Comput.*, vol. 15, nos. 3–4, pp. 179–184, 1999.
- [17] T. Soldatos, D. Karakitsos, K. Chatzimichail, M. Papathanasiou, A. Gouliamos, and A. Karabinis, "Optic nerve sonography in the diagnostic evaluation of adult brain injury," *Critical Care*, vol. 12, no. 3, p. R67, 2008.
- [18] S. A. Ballantyne, G. O'Neill, R. Hamilton, and A. S. Hollman, "Observer variation in the sonographic measurement of optic nerve sheath diameter in normal adults," *Eur. J. Ultrasound*, vol. 15, no. 3, pp. 145–149, 2002.
- [19] I. Marshall, I. MacCormick, R. Sellar, and I. Whittle, "Assessment of factors affecting MRI measurement of intracranial volume changes and elastance index," *Brit. J. Neurosurgery*, vol. 22, no. 3, pp. 389–397, 2008.
- [20] C. R. De Weese and R. W. Olson, "Pressure capacitance transducer," U.S. Patent 2907320, Oct. 6, 1959.
- [21] R. R. Schaberg and J. E. Cole, "Disposable physiological pressure sensing system," U.S. Patent 4545389, Oct. 8, 1985.
- [22] T. Y. Chang *et al.*, "Cell and protein compatibility of parylene-C surfaces," *Langmuir*, vol. 23, no. 23, pp. 11718–11725, 2007.
- [23] K. K. Ooi and A. J. Acosta, "The utilization of specially tailored air bubbles as static pressure sensors in a jet," *J. Fluids Eng.*, vol. 106, no. 4, pp. 459–465, 1984.
- [24] B. Ran and J. Katz, "The response of microscopic bubbles to sudden changes in the ambient pressure," *J. Fluid Mech.*, vol. 224, pp. 91–115, Mar. 1991.
- [25] J. D. Suter, C. J. Hohimer, J. M. Fricke, J. Christ, H. Kim, and A. T. Evans, "Principles of meniscus-based MEMS gas or liquid pressure sensors," *J. Microelectromech. Syst.*, vol. 22, no. 3, pp. 670–677, Jun. 2013.
- [26] N. Srivastava and M. A. Burns, "Microfluidic pressure sensing using trapped air compression," *Lab Chip*, vol. 7, no. 5, pp. 633–637, 2007.
- [27] C. D. Lee, "Strategies for improving mechanical and biochemical interfaces between medical implants and tissues," Ph.D. dissertation, Dept., Biomed. Eng., Univ. Southern California, Los Angeles, CA, USA, 2015.
- [28] C. Y. Shih, T. A. Harder, and Y. C. Tai, "Yield strength of thin-film parylene-C," *Microsyst. Technol.*, vol. 10, no. 5, pp. 407–411, 2004.
- [29] G. Son, V. K. Dhir, and N. Ramanujapu, "Dynamics and heat transfer associated with a single bubble during nucleate boiling on a horizontal surface," *J. Heat Transf.*, vol. 121, no. 3, pp. 623–631, 1999.
- [30] S. F. Jones, G. M. Evans, and K. P. Galvin, "Bubble nucleation from gas cavities—A review," *Adv. Colloid Interface Sci.*, vol. 80, no. 1, pp. 27–50, 1999.
- [31] P.-G. De Gennes, F. Brochard-Wyart, and D. Quéré, *Capillarity and Wetting Phenomena: Drops, Bubbles, Pearls, Waves*. New York, NY, USA: Springer, 2013.
- [32] D. A. Ateya, A. A. Shah, and S. Z. Hua, "Impedance-based response of an electrolytic gas bubble to pressure in microfluidic channels," *Sens. Actuators, A, Phys.*, vol. 122, no. 2, pp. 235–241, 2005.
- [33] R. G. Ehl and A. J. Ihde, "Faraday's electrochemical laws and the determination of equivalent weights," *J. Chem. Edu.*, vol. 31, no. 5, p. 226, 1954.
- [34] S. Z. Hua, F. Sachs, D. X. Yang, and H. D. Chopra, "Microfluidic actuation using electrochemically generated bubbles," *Anal. Chem.*, vol. 74, no. 24, pp. 6392–6396, 2002.
- [35] A. W. Adamson and A. P. Gast, *Physical Chemistry of Surfaces*. Hoboken, NJ, USA: Wiley, 1967.
- [36] L. Liebermann, "Air bubbles in water," *J. Appl. Phys.*, vol. 28, no. 2, pp. 205–211, 1957.
- [37] P. S. Epstein and M. S. Plesset, "On the stability of gas bubbles in liquid-gas solutions," *J. Chem. Phys.*, vol. 18, no. 11, pp. 1505–1509, 1950.
- [38] J. E. B. Randles, "Kinetics of rapid electrode reactions," *Discussions Faraday Soc.*, vol. 1, pp. 11–19, Mar. 1947.
- [39] C. A. Gutierrez and E. Meng, "A subnanowatt microbubble pressure sensor based on electrochemical impedance transduction in a flexible all-parylene package," in *Proc. 24th IEEE Int. Conf. Micro Electro Mech. Syst. (MEMS)*, Cancún, Mexico, Jan. 2011, pp. 549–552.
- [40] C. A. Gutierrez, C. McCarty, B. Kim, M. Pahwa, and E. Meng, "An implantable all-parylene liquid-impedance based MEMS force sensor," in *23rd IEEE Int. Conf. Micro Electro Mech. Syst., Tech. Dig. (MEMS)*, New York, NY, USA, Jan. 2010, pp. 600–603.
- [41] E. Meng and Y.-C. Tai, "Parylene etching techniques for microfluidics and bioMEMS," in *Proc. 18th IEEE Int. Conf. Micro Electro Mech. Syst. (MEMS)*, Jan./Feb. 2005, pp. 568–571.
- [42] B. J. Kim, C. A. Gutierrez, G. A. Gerhardt, and E. Meng, "Parylene-based electrochemical-MEMS force sensor array for assessing neural probe insertion mechanics," in *Proc. IEEE 25th Int. Conf. Micro Electro Mech. Syst. (MEMS)*, Jan./Feb. 2012, pp. 124–127.
- [43] I. Leusen, "Regulation of cerebrospinal fluid composition with reference to breathing," *Physiol. Rev.*, vol. 52, no. 1, pp. 1–56, 1972.
- [44] B. K. Siesjö, "The regulation of cerebrospinal fluid pH," *Kidney Int.*, vol. 1, pp. 360–374, 1972.
- [45] N. P. Brandon and G. H. Kelsall, "Growth kinetics of bubbles electrogenerated at microelectrodes," *J. Appl. Electrochem.*, vol. 15, no. 4, pp. 475–484, 1985.
- [46] P.-Y. Li, R. Sheybani, C. A. Gutierrez, J. T. W. Kuo, and E. Meng, "A parylene bellows electrochemical actuator," *J. Microelectromech. Syst.*, vol. 19, no. 1, pp. 215–228, Feb. 2010.
- [47] E. Ruckenstein and E. J. Davis, "The effects of bubble translation on vapor bubble growth in a superheated liquid," *Int. J. Heat Mass Transf.*, vol. 14, no. 7, pp. 939–952, 1971.
- [48] O. R. Enriquez *et al.*, "Growing bubbles in a slightly supersaturated liquid solution," *Rev. Sci. Instrum.*, vol. 84, no. 6, p. 065111, 2013.



**Lawrence Yu** received the B.S. degree in biomedical engineering and the M.S. degree in electrical engineering from the University of Southern California (USC), Los Angeles, in 2009 and 2010, respectively, where he is currently pursuing the Ph.D. degree in biomedical engineering with the USC Biomedical Microsystems Laboratory. He is currently working on the development of a sensor platform for *in vivo* applications. He was a recipient of the Walt Disney Foundation Scholarship and the Rose Hills Foundation Fellowship.



**Christian A. Gutierrez** received the B.S. degrees in electrical engineering and business economics and management, in 2005; the M.S. degree in electrical engineering from the California Institute of Technology (Caltech), Pasadena, in 2006; and the Ph.D. degree in biomedical engineering from the University of Southern California, Los Angeles, in 2011. He conducted research with the National Science Foundation's Biomimetic Microelectronic Systems Engineering Research Center and the USC Biomedical Microsystems Laboratory toward the develop-

ment of novel impedance-based micro- and nanotechnologies for biomedical applications and focused specifically on the development of retinal prosthesis technologies to restore sight to the blind. While at the Caltech Micromachining Laboratory, he worked on identifying, analyzing, and implementing power harvesting and storage circuitry for microelectromechanical systems-based power harvesting devices. He is the Co-Founder and Chief Technology Officer with Fluid Synchrony LLC, which develops high performance implantable micropump technology for drug delivery applications. He was a recipient of the Caltech Presidential Scholarship, the Bill and Melinda Gates Millennium Fellowship, and the USC Viterbi School of Engineering Kunzel Fellowship.



**Ellis Meng** (M'02–SM'09) received the B.S. degree in engineering and applied science, and the M.S. and Ph.D. degrees in electrical engineering from the California Institute of Technology (Caltech), Pasadena, in 1997, 1998 and 2003, respectively. She is currently a Professor and the Chair of the Department of Biomedical Engineering with the University of Southern California, Los Angeles, where she has been since 2004. She also holds a joint appointment with the Ming Hsieh Department of Electrical Engineering. Her research interests include bioMEMS,

implantable biomedical microdevices, microfluidics, multimodality integrated microsystems, and packaging. She held the Viterbi Early Career Chair with the Viterbi School of Engineering. She is a Member of Tau Beta Pi, the Biomedical Engineering Society, the Society of Women Engineers, and the American Society for Engineering Education. She was a recipient of the Intel Women in Science and Engineering Scholarship, the Caltech Alumni Association Donald S. Clark Award, and the Caltech Special Institute Fellowship. She has also received the NSF CAREER and Wallace H. Coulter Foundation Early Career Translational Research Awards. In 2009, she was recognized as one of the TR35 Technology Review Young Innovators under 35.